

Seasonal fluctuations of the surface North Equatorial Countercurrent (NECC) across the Pacific basin

Yi-Chia Hsin¹ and Bo Qiu¹

Received 30 November 2011; revised 19 April 2012; accepted 20 April 2012; published 1 June 2012.

[1] Based on multisatellite-derived sea surface current, sea surface height anomaly, and geostrophic current data, the annual variability of the surface NECC across the Pacific basin is investigated. Inferred from the surface current data, the NECC axis east and west of the dateline moves northward along its pathway in the latter half of a year and the first half of a year, respectively. The sea surface height anomaly in the NECC region and the meridional movement of NECC are well reproduced by a linear wind-driven first-mode baroclinic Rossby wave model. Model experiments by setting the phase speed of baroclinic Rossby wave or the Ekman pumping to zero in different regions are carried out to clarify the influence of Rossby wave and local Ekman pumping on the movement of NECC. East of the dateline, both Ekman pumping and Rossby wave are important in determining the northward movement of the NECC axis. However, the NECC axis west of the dateline moves northward primarily due to the westward transmission of positive sea surface height anomalies (or downwelling Rossby waves) that originate in the east of the dateline. The local Ekman pumping plays a minor role in controlling the migration of the NECC axis west of the dateline.

Citation: Hsin, Y.-C., and B. Qiu (2012), Seasonal fluctuations of the surface North Equatorial Countercurrent (NECC) across the Pacific basin, *J. Geophys. Res.*, *117*, C06001, doi:10.1029/2011JC007794.

1. Introduction

[2] The North Equatorial Countercurrent (NECC), flowing eastward across the tropical Pacific Ocean between 2°N and 10°N, can be regarded as a boundary between the North and South Pacific tropical gyres [Wyrki and Kendall, 1967; Philander *et al.*, 1987; Reverdin *et al.*, 1994; Donguy and Meyers, 1996]. Originating in the western Pacific, it is fed by the mainstream of Mindanao Current, the branch of Mindanao Current retroflecting cyclonically in the Celebes Sea, and the South Equatorial Current [Lukas *et al.*, 1991]. It plays an important role in transporting the convergent surface warm water from the western Pacific warm pool to the eastern tropical Pacific Ocean [Philander *et al.*, 1987]. The warm water advected by the NECC from the west has further been suggested to be one of the factors resulting in the equatorial asymmetry of InterTropical Convergence Zone (ITCZ) in the eastern Pacific [Richards *et al.*, 2009; Masunaga and L'Ecuyer, 2011].

[3] Based on in situ observations scattered in time and space, the mean NECC transport in the western Pacific Ocean has been observed at a wide range of 0–90 Sv [Wyrki

and Kendall, 1967; Delcroix *et al.*, 1987, 1992; Qiu and Joyce, 1992; Donguy and Meyers, 1996; Johnson *et al.*, 2002]. As the NECC flows eastward, its mean transport decreases from larger than 30 Sv in the west to less than 10 Sv in the east [e.g., Wyrki and Kendall, 1967; Philander *et al.*, 1987; Gouriou and Toole, 1993; Donguy and Meyers, 1996; Johnson *et al.*, 2002; Brown *et al.*, 2007; Richards *et al.*, 2009], its main axis shifts northward [Reverdin *et al.*, 1994; Yu *et al.*, 2000; Johnson *et al.*, 2002], and its depth shoals from 110 to 40 m [Johnson *et al.*, 2002; Sprintall *et al.*, 2009].

[4] In terms of seasonality, the observed NECC transport is smaller in boreal winter–spring and larger in summer–fall [Wyrki and Kendall, 1967; Wyrki, 1974; Delcroix *et al.*, 1987; Qiu and Joyce, 1992; Gouriou and Toole, 1993; Reverdin *et al.*, 1994; Donguy and Meyers, 1996; McPhaden, 1996; Coles and Rienecker, 2001; Bonjean and Lagerloef, 2002; Johnson *et al.*, 2002; Heron *et al.*, 2006]. From the results of hydrographic casts, surface drifters, and current meter records, the NECC width is broader (narrower) with a southern (northern) core in spring (fall) [Reverdin *et al.*, 1994; Johnson *et al.*, 2002]. In addition, Johnson *et al.* [2002] found that the NECC is strongest in October–December west of 125°W and in August at 95°W according to the 15-year (1985–2000) Conductivity Temperature Depth/Acoustic Doppler Current Profiler (CTD/ADCP) measurements between 138°E and 86°W, indicating a westward phase propagation of the seasonal NECC transport signals. The zonal-current-weighted latitude in their study also reveals that the NECC is located furthest to the south (north) when its transport is at a seasonal minimum (maximum).

¹Department of Oceanography, University of Hawai'i at Mānoa, Honolulu, Hawaii, USA.

Corresponding author: Y.-C. Hsin, Department of Oceanography, University of Hawai'i at Mānoa, 1000 Pope Rd., Honolulu, HI 96822, USA. (yichia@hawaii.edu)

This paper is not subject to U.S. copyright.
Published in 2012 by the American Geophysical Union.

Furthermore, they suggested that the NECC is warmest and freshest when it has the seasonally largest transport.

[5] The existing studies have attributed the seasonal change of NECC to two factors. The first is the annual meridional shift of the ITCZ, which reaches the northernmost latitude during boreal summer and fall when the positive Ekman pumping velocity shifts northward in the Tropics [Philander *et al.*, 1987; Donguy and Meyers, 1996; Qiu and Lukas, 1996; Coles and Rienecker, 2001; Johnson *et al.*, 2002]. The second factor is the westward-propagating annual equatorial Rossby waves, starting from boreal autumn (or spring) in the eastern tropical Pacific [Yu and McPhaden, 1999; Ando and Hasegawa, 2009]. These first-mode baroclinic upwelling (downwelling) Rossby waves result in a westward (eastward) flow anomaly that weakens (reinforces) the NECC [Delcroix *et al.*, 1991]. Thus, a linear wind-driven Rossby wave model has been extensively adopted in exploring the dynamics of currents in the off-equatorial regions (usually $> \pm 3^\circ$) [e.g., White, 1977; Meyers, 1979; Kessler, 1990; Qiu and Joyce, 1992; Chen and Qiu, 2004; Kessler, 2006; Qiu and Chen, 2010].

[6] Although many observational studies have focused on the NECC, only one paper [Johnson *et al.*, 2002] covered its entire geographical domain and gave the most complete descriptions and discussions to date. In spite of their efforts, the NECC remains one of the least frequently sampled equatorial surface currents. Considerable new in situ and satellite measurements of the NECC have become available over the past decade. This motivates us to re-examine the NECC seasonality and to clarify its underlying dynamics across the entire Pacific basin. There are two objectives in the present study. The first objective is to describe in detail the seasonal variation of the surface NECC, including its position and strength, across the entire tropical Pacific with the use of the Ocean Surface Current Analysis - Real Time product (OSCAR) and altimeter-based geostrophic currents. One of the new findings revealed in the present study is that the seasonal position of NECC shifts differently along its mean pathway east and west of the dateline. The second objective is to use a linear wind-driven first-mode baroclinic Rossby wave model to clarify the newly observed seasonality. The paper is structured as follows. The data and dynamic quantities used in the study are introduced and defined in section 2. Description of the linear wind-driven first-mode baroclinic Rossby wave model is given in section 3. Section 4 presents the NECC seasonality based on the OSCAR and altimeter-based geostrophic currents. Section 5 presents the relevant dynamic discussions, and the final section summarizes the conclusions.

2. Data and Methodology

2.1. The OSCAR and Altimetric Data

[7] The OSCAR data is derived from multisatellite data and is obtained from the Physical Oceanography Distributed Active Archive Center at the National Aeronautics and Space Administration Jet Propulsion Laboratory (PO.DACC/NASA JPL, <http://podaac.jpl.nasa.gov/>). It is developed by the Earth and Space Research (ESR) [Bonjean and Lagerloef, 2002; Johnson *et al.*, 2007]. With combined use of the altimeter-based sea surface height anomaly (SSHA), sea surface scatterometer wind, sea surface temperature

(SST), and mean dynamic topography, the near-surface flows are computed based on the geostrophic, Ekman, and Stommel shear dynamics. The gridded SSHA has a horizontal resolution of $1/3^\circ$ and is derived from the merged satellite altimeter data of TOPEX/Poseidon, Jason-1&2, ERS-1&2, GFO, and ENVISAT by AVISO (Archiving, Validation and Interpretation of Satellite Oceanographic data). The absolute sea surface height (SSH) field is obtained by adding the mean dynamic topography (RioMDT) of Rio and Hernandez [2004] to SSHA. The sea surface winds are from the Special Sensor Microwave Imager (SSM/I) for the period before July 1999, from QuikSCAT for the period between August 1999 and November 2009, and from National Centers for Environmental Prediction for the period after December 2009. To evaluate the buoyancy force in the surface current formulation, the Reynolds and Smith version 2 SST, which blends the AVHRR (Advanced Very High Resolution Radiometer) and in situ data, is adopted [Reynolds *et al.*, 2002]. More descriptions about the OSCAR product can be found in Bonjean and Lagerloef [2002], Johnson *et al.* [2007], and the OSCAR handbook (http://opendap.jpl.nasa.gov/opendap/allData/oscar/preview/L4/oscar_third_deg/docs/oscarthirdguide.pdf).

[8] Two versions of OSCAR products can be obtained from the PO.DACC/NASA JPL: a 1° version and a $1/3^\circ$ version. Both versions are compiled at an interval of 5 days and available from October 1992, when the TOPEX/Poseidon was launched, to the present. Some improvements (compared to the prior studies of Bonjean and Lagerloef [2002] and Johnson *et al.* [2007]) are made in the latest OSCAR product. One major improvement is to integrate the AVISO SSHA gridded product into the processing. The other one concerns the geostrophic equatorial treatment in which the β -plane approximation is adopted in the equatorial region between 5°N and 5°S (8°N – 8°S was used in Bonjean and Lagerloef [2002]). Eighteen years of data from October 1992 to September 2010 are used in our analyses. By comparing both versions of the OSCAR products with the observed velocities of mooring current meters, we find that the 1° OSCAR is superior to the $1/3^\circ$ one (see Appendix A for detailed comparison). Thus, the 1° OSCAR will be used in the following analyses.

[9] For comparison with the results from the OSCAR product, we also use the AVISO SSHA and absolute SSH products in this study. The original $1/3^\circ$ AVISO product is re-gridded to the 1° OSCAR grid by averaging over nine adjacent grid points and is referred to below as AVISO-SSHA and AVISO-SSH, respectively.

2.2. Geostrophic Current

[10] The surface geostrophic velocities are derived from AVISO-SSH using the following geostrophic balance:

$$U_g(x, y, t) = -\frac{g}{f(y)} \frac{\partial h(x, y, t)}{\partial y}, \quad (1)$$

$$V_g(x, y, t) = \frac{g}{f(y)} \frac{\partial h(x, y, t)}{\partial x}, \quad (2)$$

where U_g and V_g are the zonal and meridional components of the surface geostrophic current, respectively, x and y are

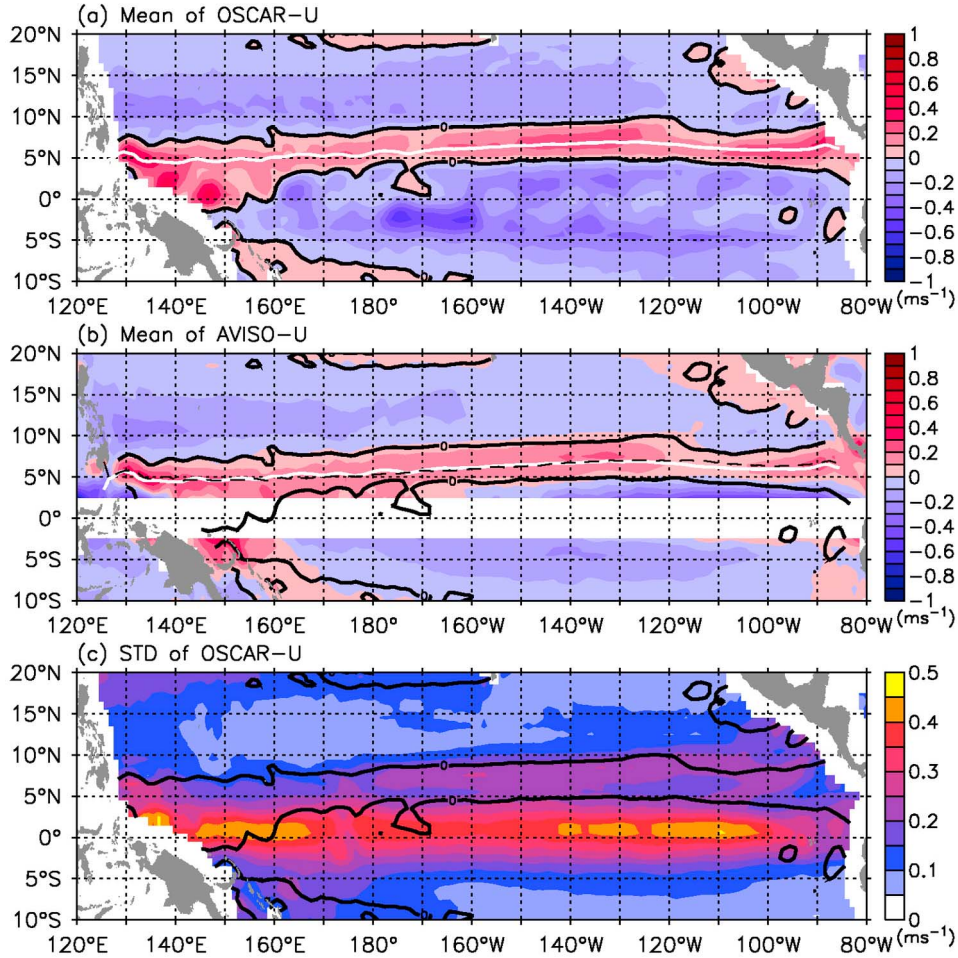


Figure 1. Mean zonal velocities of (a) OSCAR surface current (OSCAR-U) and (b) AVISO-based geostrophic current (AVISO-U), and (c) standard deviations (STD) of OSCAR-U. The mean and STD are calculated using current data in the period between October 1992 and September 2010. The white line in Figures 1a and 1b denotes the mean OSCAR-U-based Y_{CM} , and the black dashed line in Figure 1b is the mean AVISO-U-based Y_{CM} . The black solid lines are the zero contour of mean OSCAR-U.

longitude and latitude, h is the absolute SSH, g is the gravitational acceleration, $f(y) = 2\Omega\sin(y)$ is the Coriolis parameter, and Ω is the angular velocity of the Earth's rotation. The central finite difference scheme is adopted for the calculation of equations (1) and (2). Here, the surface geostrophic current is only calculated in the region north of 2°N because $f(y)$ approaches zero near the equator.

2.3. Center of NECC

[11] In this study, we use the conception of “center of mass” to define the center of NECC as follows:

$$Y_{CM}(x, t) = \frac{\int_{Y_S}^{Y_N} y \cdot u(x, y, t) dy}{\int_{Y_S}^{Y_N} u(x, y, t) dy}, \quad (3)$$

where Y_{CM} denotes the position of NECC center in degrees, Y_N and Y_S are the northern and southern limits of integration, and u is the zonal velocity (which can be the near-surface velocity or altimeter-based geostrophic velocity), and is set to zero for negative u because the NECC is thought of as an eastward flow.

[12] Averaged over the period between October 1992 and September 2010, the mean Y_{CM} is depicted by the white curve in Figure 1a. The mean Y_{CM} in general follows the core of mean NECC. For equation (3), we adopt 10°N and 2°N as Y_N and Y_S to calculate the mean Y_{CM} . The mean Y_{CM} value does not change significantly when Y_N is shifted northward to 12°N or when Y_S is shifted southward to the equator.

2.4. Intensity of NECC

[13] To examine the amount of mass carried by the NECC, we define the NECC intensity as

$$INT(x, t) = \int_{\max(Y_{CM}-4^\circ, 2^\circ\text{N})}^{Y_{CM}+4^\circ} u(x, y, t) dy, \quad (4)$$

where Y_{CM} is given by equation (3). As in equation (3), u is set to zero if it is negative. The integral width of $\pm 4^\circ$ is adopted because the mean NECC spans a range of about 8° between 2°N and 10°N (see section 4.1). In addition, because the geostrophic current is calculable only for the

area north of 2°N , the southern limit for integration of INT is set to $\max(Y_{CM} - 4^\circ, 2^\circ\text{N})$.

3. Linear Wind-Driven First-Mode Baroclinic Rossby Wave Model

[14] Under the longwave approximation, the governing equation of the linear wind-driven first-mode baroclinic Rossby wave model (with zero background flow) is given by [e.g., Meyers, 1979; Kessler, 1990]

$$\frac{\partial h'(x, y, t)}{\partial t} - C_R(x, y) \frac{\partial h'(x, y, t)}{\partial x} = - \frac{g'}{g\rho_0} \nabla \times \frac{\vec{\tau}(x, y, t)}{f(y)} \cdot \vec{k} - \varepsilon h'(x, y, t), \quad (5)$$

where h' is SSHA, $C_R = \beta(y)C_1(x, y)^2/f(y)^2$ is the phase speed of the first-mode baroclinic Rossby wave, $\beta(y)$ is the meridional derivative of the Coriolis parameter, C_1 is the phase speed of the first-mode baroclinic gravity wave, g' is the reduced gravity, ρ_0 is the reference density, ε is the Newtonian dissipation rate, $\vec{\tau}$ is the wind stress vector, and \vec{k} is the unit normal in vertical direction. By integrating equation (5) from the eastern boundary ($x = x_e$) along the characteristic of the baroclinic Rossby wave, h' has an analytic solution of

$$h'_m(x, y, t) = \frac{g'}{g\rho_0} \int_{x_e}^x \frac{1}{C_R(x', y)} \nabla \times \frac{\vec{\tau}(x', y, t + \frac{(x-x')}{C_R(x', y)})}{f(y)} \cdot \vec{k} e^{\frac{\varepsilon(x-x')}{C_R(x', y)}} dx', \quad (6)$$

where h'_m denotes the modeled SSHA deduced from the wind-driven first-mode baroclinic Rossby wave model, and x' is longitude. In equation (6), g and ρ_0 are set to the constants of 9.807 m s^{-2} and 1025 kg m^{-3} , respectively, and C_R is evaluated from the global climatological atlas of first-mode baroclinic gravity wave compiled by Chelton *et al.* [1998].

[15] In equation (6), the modeled SSHA is a function of g' and ε when other parameters are given. It is linearly proportional to g' and has a more complicated dependence on ε . In order to obtain the suitable g' and ε values, a quantity representing the sum of absolute difference between the AVISO-SSHA and modeled SSHA along a parallel is defined as

$$D(y, \varepsilon, g') = \sum_{x=x_w}^{x=x_e} \sum_{t=T_1}^{t=T_2} |\eta_{AVISO}(x, y, t, \varepsilon, g') - \eta_{MODEL}(x, y, t, \varepsilon, g')|, \quad (7)$$

where η_{AVISO} and η_{MODEL} are the AVISO-SSHA and modeled SSHA, respectively; T_1 is January 1993 and T_2 is December 2009; x_e and x_w are the eastern and western edges of Pacific. The optimal g' and ε values can be determined by finding the minimum of D along a latitude with $1/\varepsilon = 0\text{--}5$ years and $g' = 0\text{--}0.3 \text{ kg m s}^{-1}$.

[16] The wind-forcing data used in equation (6) is the operational ocean analysis/reanalysis system produced by the European Centre for Medium Range Weather Forecast (ECMWF ORA-S3) [Balmaseda *et al.*, 2008]. The ECMWF ORA-S3 wind stress data has a horizontal resolution of 1° in both zonal and meridional directions and is available from January 1959 to December 2009. Modeled results between

1993 and 2009 are used in the following analyses. Other satellite-based wind products, such as the Cross-Calibrated MultiPlatform (CCMP) Ocean Surface Wind Vector Analysis Fields from the PO.DACC/NASA, are also tested, and similar results are attained.

4. Observational Results

4.1. Mean and Variance of Surface NECC

[17] The mean zonal velocity of OSCAR (OSCAR-U) is shown in Figure 1a. The positive zonal velocity (red color) between the equator and 10°N signifies the mean pathway of the eastward-flowing NECC. The width of NECC is much wider west of 160°E , while it becomes uniform in the central and eastern Pacific. In terms of the magnitude of mean NECC velocity, it can roughly be separated into three segments. The NECC decreases downstream west of 160°E , increases between 160°E and 120°W , and after a brief drop near 115°W , increases again east of 115°W , qualitatively consistent with previous findings [e.g., Johnson *et al.*, 2002].

[18] In addition to the basin-wide changes of the NECC width and strength, a poleward shift of the NECC from the west to the east can be clearly seen from the central position of NECC (Y_{CM} , white line in Figure 1a). The mean Y_{CM} , on zonal average, is about 6°N . The mean Y_{CM} is located at $4^\circ\text{N}\text{--}5^\circ\text{N}$ in the western Pacific and at $6^\circ\text{N}\text{--}7^\circ\text{N}$ in the central Pacific. In the eastern Pacific (east of 120°W), Y_{CM} moves slightly equatorward and then veers poleward again near the coast. The curvature in the eastern Pacific is related to the cyclonic Costa Rica Dome centered around 9°N , 90°W [e.g., Kessler, 2006]. The past findings of the position of NECC main axis [e.g., Reverdin *et al.*, 1994; Yu *et al.*, 2000] and the zonal-velocity-weighted latitude [Johnson *et al.*, 2002] bear out the spatial distribution of mean Y_{CM} . All of the features of NECC revealed in the OSCAR data are also seen in the AVISO-based zonal geostrophic velocity (AVISO-U, Figure 1b).

[19] Figure 1c shows the standard deviation (STD) of OSCAR-U. Large standard deviations ($>0.5 \text{ m s}^{-1}$) are seen in the western part of NECC, especially in the region south of 5°N . This result indicates that the NECC exhibits a more complicated behavior in the western Pacific. This high complexity is attributable to the NECC's multiple formation sources [Lukas *et al.*, 1991], the wind variability (monsoon or trade winds), and the meso- to sub-gyre scale eddies (e.g., Halmahera Eddy, Mindanao Eddy, Palau Eddy) [Qiu *et al.*, 1999; Heron *et al.*, 2006]. In the central and eastern Pacific, STD is reduced to less than 0.3 ms^{-1} in the NECC band. Outside the NECC band, STD north of the NECC is much reduced ($<0.2 \text{ m s}^{-1}$) while that around the equator is larger due to the prevailing equatorial waves generated on multiple timescales from intraseasonal to interannual.

[20] By means of the Fast Fourier Transform, Figure 2 shows the longitude-dependent OSCAR-U spectra averaged between 2°N and 10°N . The 120-day, semiannual, annual, 1.5-year, and 3-year signals stand out across the entire NECC region. In addition to these basin-wide fluctuating signals, signals on ~ 30 days and ~ 6 years are significant between 160°W and 110°W . The 30-day signal could be ascribed to the activity of tropical instability waves just south of the NECC [Qiao and Weisberg, 1995]. The longest

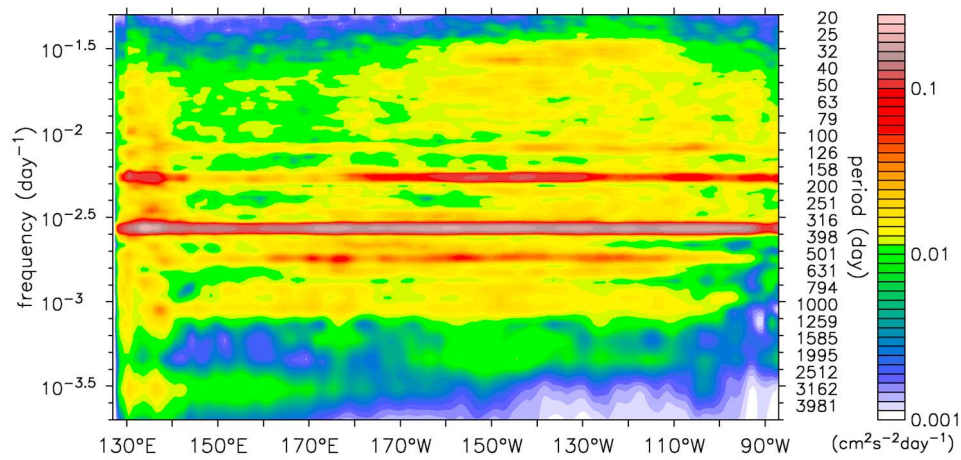


Figure 2. Longitude-specific variance-preserving spectrum of OSCAR-U averaged between 2°N and 10°N.

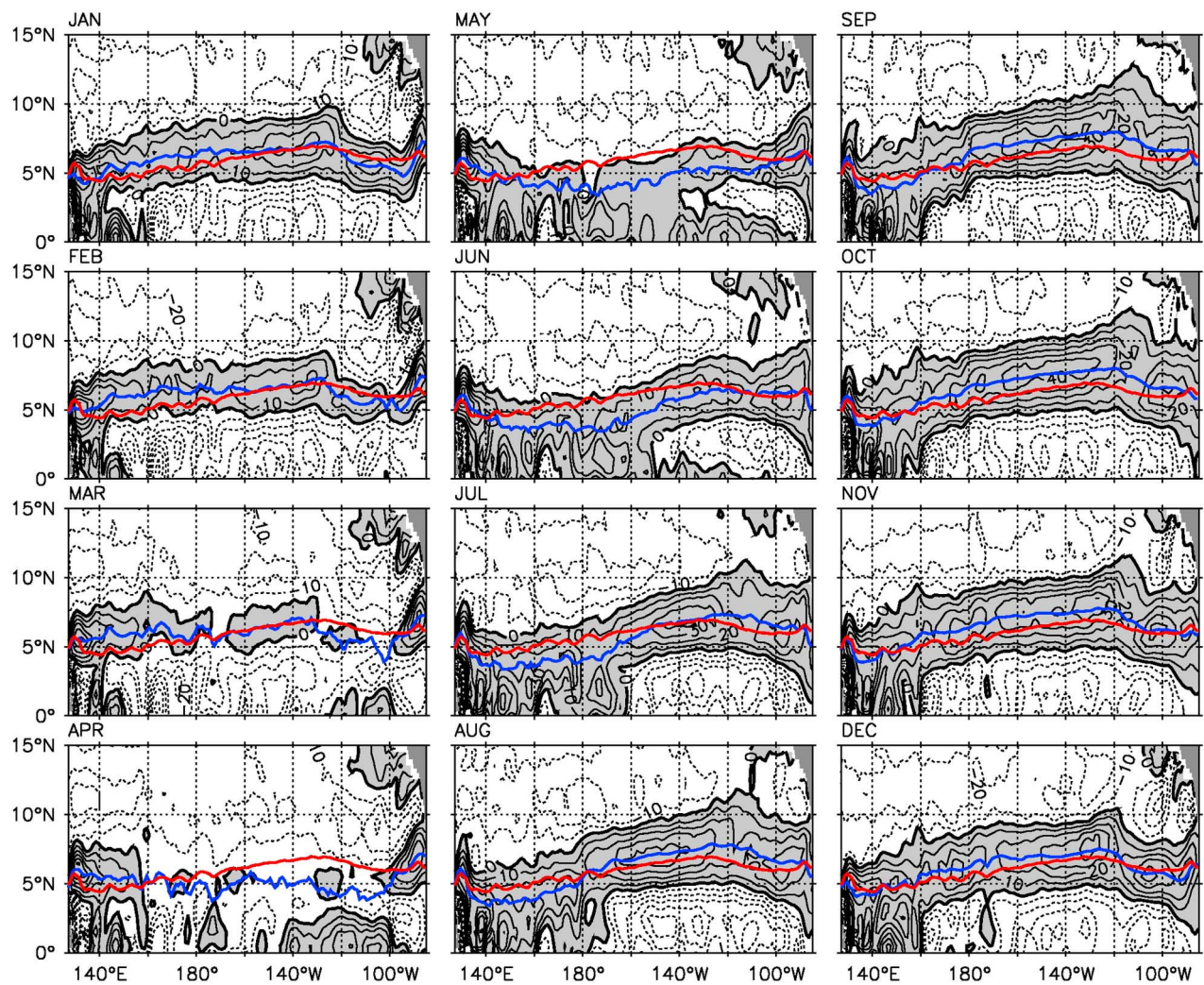


Figure 3. Monthly distribution of OSCAR-U averaged month-by-month over the period between October 1992 and September 2010. Gray shading denotes the eastward flow and contour interval is 10 cm s⁻¹. Red curve is the annual mean Y_{CM} , and blue one depicts Y_{CM} averaged over the eighteen years in each month.

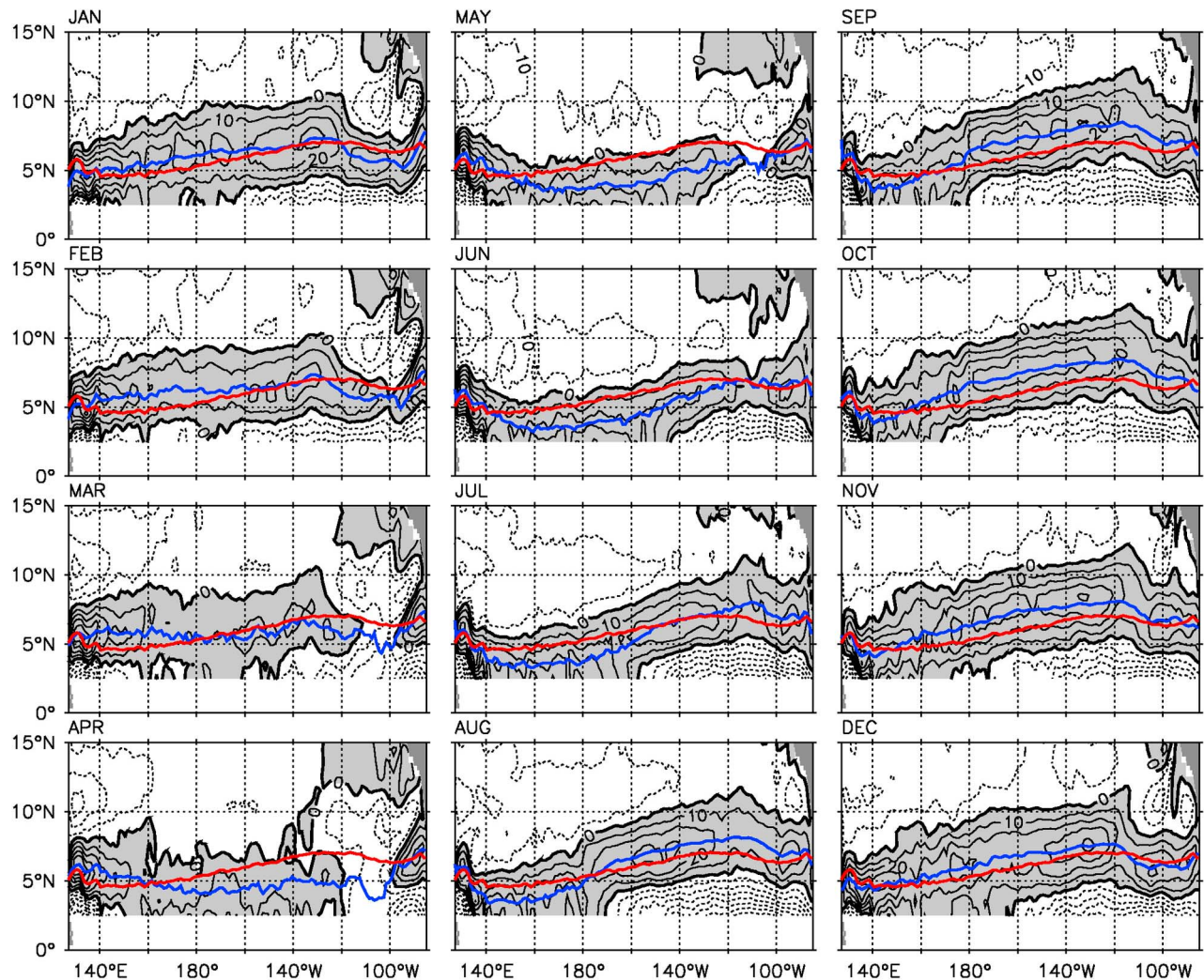


Figure 4. Same as Figure 3, but for the AVISO-U.

variability (~ 10 years) shows up only west of the dateline, reflecting the NECC's multidecadal changes in conjunction with the sea level rise in the western tropical Pacific Ocean [Qiu and Chen, 2012]. Among these signals of intraseasonal to decadal timescales, the annual peak is most dominant and extends across the whole Pacific basin. And, the 150–500-day-bandpassed OSCAR-U is accountable for about 52% of the total variance in the NECC region (2°N – 10°N , 130°E – 90°W). The result is consistent with the past studies based on the TOPEX/Poseidon SSH [Chelton *et al.*, 2003; Perez *et al.*, 2005] and thermocline depth data [Meyers, 1979; Kessler, 1990], showing that the annual signals are most energetic along 5.5°N (the center latitude of the NECC) and extend across the full width of the Pacific. Given this dominance, understanding the basin-wide annual fluctuations of the NECC will be the focus of our following analyses.

4.2. Seasonality of Surface NECC

4.2.1. Surface Flow

[21] Although Bonjean and Lagerloef [2002] have presented the seasonally varying surface flow using the

previously available 1° OSCAR, their focus was on the currents along the equator. With the improvement of the SSH product, we will update the work of Bonjean and Lagerloef [2002] and focus on the NECC band. Figure 3 shows the annual march of OSCAR-U encompassing the NECC region. The gray color denotes the eastward flow. Across the entire Pacific basin, the NECC has the broadest width in September–October. In March–April, the NECC is weakest and discontinuous in the eastern Pacific and almost disappears in the central Pacific. By June, it revives and has the southernmost position in the central Pacific. The NECC in the central and eastern Pacific gains its highest speed ($>40 \text{ cm s}^{-1}$) in October when it reaches the northernmost position. It progressively weakens afterwards. The seasonal changes of NECC position and intensity in the central and eastern Pacific (e.g., NECC strongest/furthest north in fall) are consistent with the historical observations [Reverdin *et al.*, 1994; Donguy and Meyers, 1996; Johnson *et al.*, 2002]. Regarding the NECC in the western Pacific, its eastward flow appears all year-round with the strongest (weakest) velocity in July (January). In the western Pacific, the NECC is directed to the east in November–April and to

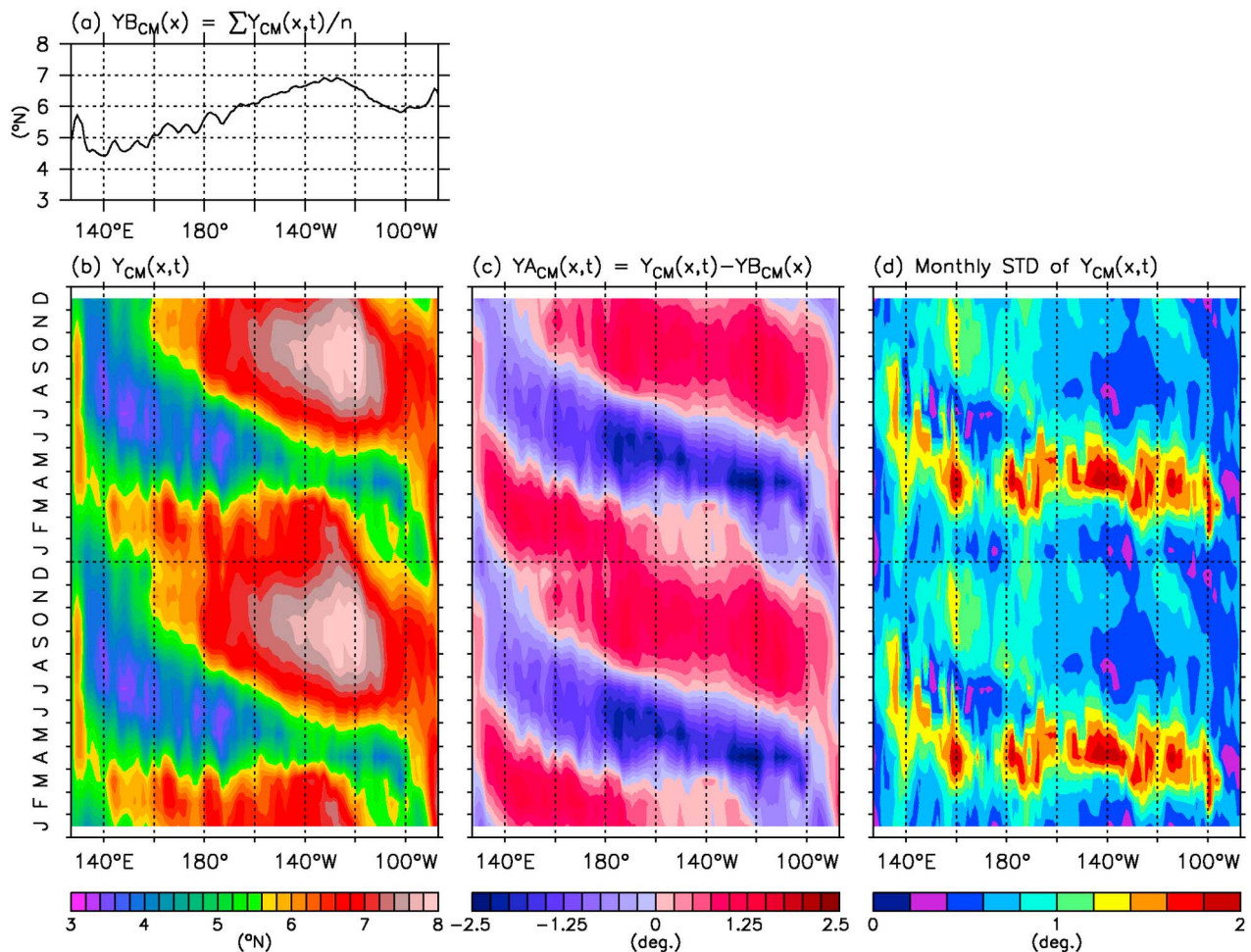


Figure 5. (a) OSCAR-U-based mean Y_{CM} averaged over the period from October 1992 to September 2010. Averaging month-by-month instead from October 1992 to September 2010, the monthly distribution of (b) Y_{CM} , (c) anomaly of Y_{CM} , and (d) standard deviation of Y_{CM} are shown.

the southeast during the rest period, in good agreement with the past findings [Toole *et al.*, 1988; Heron *et al.*, 2006].

[22] Similar seasonal changes of the NECC are found in AVISO-U (Figure 4). Discrepancies also exist between OSCAR-U and AVISO-U. For example, AVISO-U has a broader width and a smaller maximal velocity of the NECC than OSCAR-U in most months. The largest difference between the two flow patterns is found in March–May. Part of this difference is likely due to the fact that OSCAR-U includes not only the geostrophic current but also the Ekman flow.

4.2.2. Center of NECC

[23] The meridional shift of NECC on the seasonal time-scale is further investigated by its central latitude, i.e., the velocity-weighted latitude, Y_{CM} . Presented in Figure 5 are the monthly distributions of longitude-dependent Y_{CM} , its anomalies ($Y_{A_{CM}}$), and standard deviations. The mean Y_{CM} ($Y_{B_{CM}}$) shown in Figure 5a is the same as the white curve in Figure 1. Generally, Y_{CM} reaches the northernmost position (up to 8°N) during September–November east of the dateline and during February–March between 140°E and 180°E (Figure 5b). It is further revealed from the $Y_{A_{CM}}$ that the northward migration of Y_{CM} undergoes different seasonal

changes in the east and west of the dateline. Y_{CM} in the east of the dateline migrates northward in the latter half of a year, whereas Y_{CM} in the west of the dateline moves northward in the first half of a year. Both of these two migrations are accompanied by westward propagating signals with speed consistent with the first-mode baroclinic Rossby waves (see detailed discussions in section 5).

[24] In terms of its monthly STD shown in Figure 5d, Y_{CM} is more variable across the entire Pacific basin during February–May when the NECC is weaker and located closer to the equator. This indicates that the NECC has stronger intraseasonal or interannual variations during February–May. Shifting the northern limit, Y_N , northward to 12°N or the southern limit, Y_S , to the equator does not alter the outcome of the seasonal change of the NECC. In addition, Y_{CM} calculated from AVISO-U well reproduces the spatial distribution and temporal evolution of the OSCAR-U-based Y_{CM} , including its position and anomaly (figures not shown).

4.2.3. Intensity of NECC

[25] Figure 6 shows the monthly distribution of intensity of NECC (INT) integrated in the latitudinal band between $\max(Y_{CM} - 4^\circ, 2^\circ\text{N})$ and $Y_{CM} + 4^\circ$. The mean INT (INTB) is

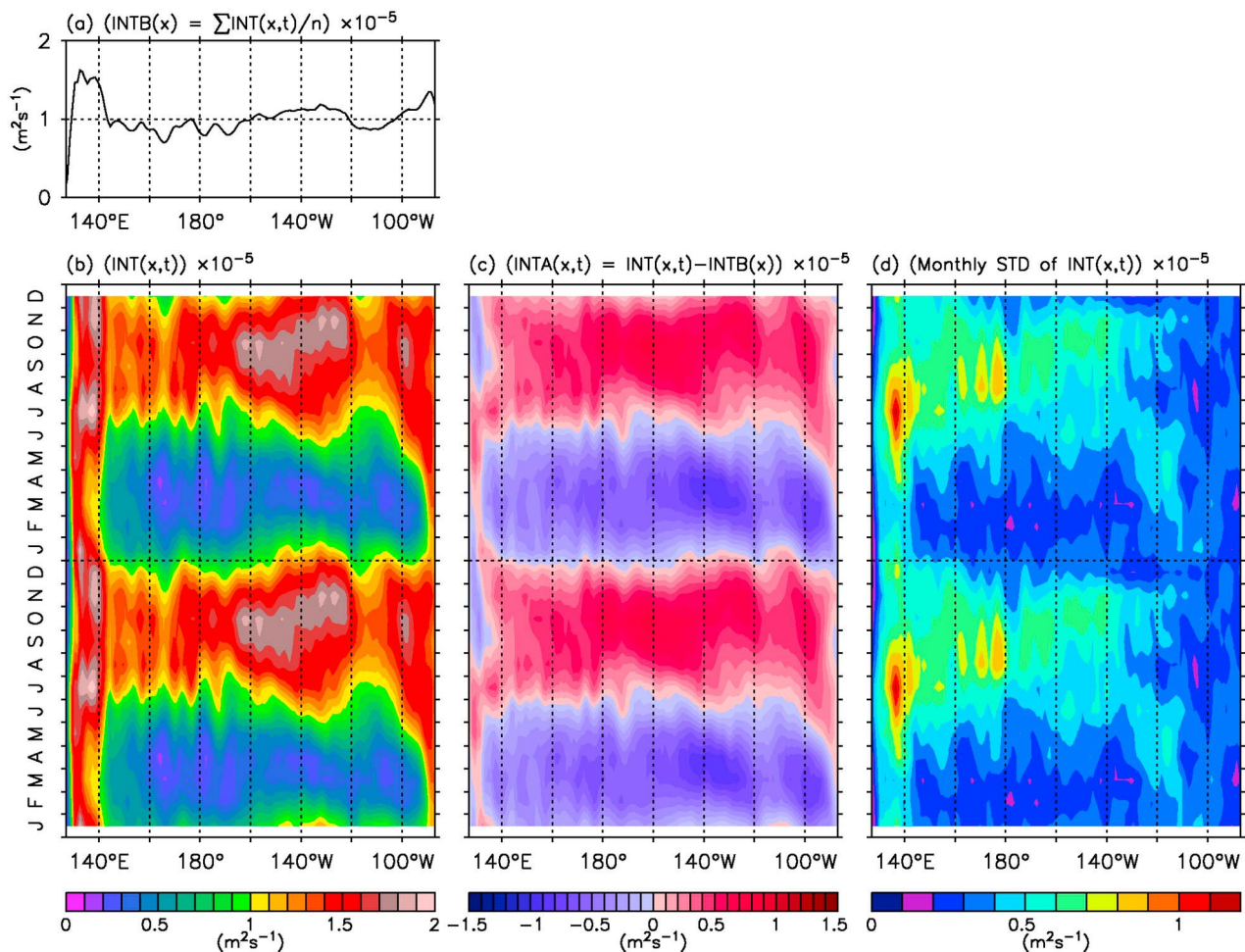


Figure 6. Same as Figure 5, but for the OSCAR-U-based NECC intensity integrated meridionally from $\max(Y_{CM} - 4^\circ, 2^\circ\text{N})$ to $Y_{CM} + 4^\circ$.

larger in the regions west of 140°E , around 140°W , and east of 100°W (Figure 6a). Unlike Y_{CM} , INT and INT anomaly (INTA) show no clear westward propagation (Figures 6b and 6c). Nor do they show an out-of-phase seasonal cycle east and west of the dateline. This is because the NECC intensity is defined in coordinate system following the migrating NECC, whereas Y_{CM} is defined in Eulerian coordinates and the Eulerianly defined Y_{CM} absorbs the westward propagating signals. Across the basin except for west of 135°E and east of 90°W , the NECC intensifies in the latter half of a year with maxima around October and weakens in the first half of a year. In terms of the monthly STD of INT (Figure 6d), its amplitude decreases from the west ($\sim 1.5 \times 10^5 \text{ m}^2 \text{ s}^{-1}$) to the east ($< 0.5 \times 10^5 \text{ m}^2 \text{ s}^{-1}$). In general, occurrence of a larger variance is accompanied with a stronger NECC.

[26] Comparing the OSCAR-U-based INTB (Figure 6a) with the AVISO-U-based INTB (Figure 7a) indicates that the magnitude of AVISO-U-based INTB is significantly smaller than the OSCAR-U-based INTB in the western and eastern Pacific. This implies that the wind can significantly strengthen the eastward flow in this region. Except for this discrepancy in the western and eastern Pacific, the seasonal

evolution of AVISO-U-based INT agrees in general with the OSCAR-U-based INT.

5. Dynamical Interpretation by Rossby Wave Model

[27] The westward propagating signals revealed in Figure 5c points to the importance of oceanic adjustment in the seasonal changes of the NECC center. As indicated in section 1, Rossby wave propagation and wind variability are the two major factors controlling the seasonal variation of NECC. The impact of these two factors can be demonstrated in the monthly distributions of SSHA and Ekman pumping velocity

$$\left(W_{EK} = \frac{1}{\rho_0} \nabla \times \left(\frac{\vec{\tau}}{f} \right) \cdot \vec{k} \right) \text{ fields.}$$

The annual march of AVISO-SSHA encompassing the NECC region is depicted in Figure 8. The OSCAR-U-based $Y_{B_{CM}}$ (red curve) and monthly Y_{CM} (blue curve) are superposed in the figure to discuss the relationship between the meridional movement of NECC and the SSH changes. Close relationship is found between them across the entire

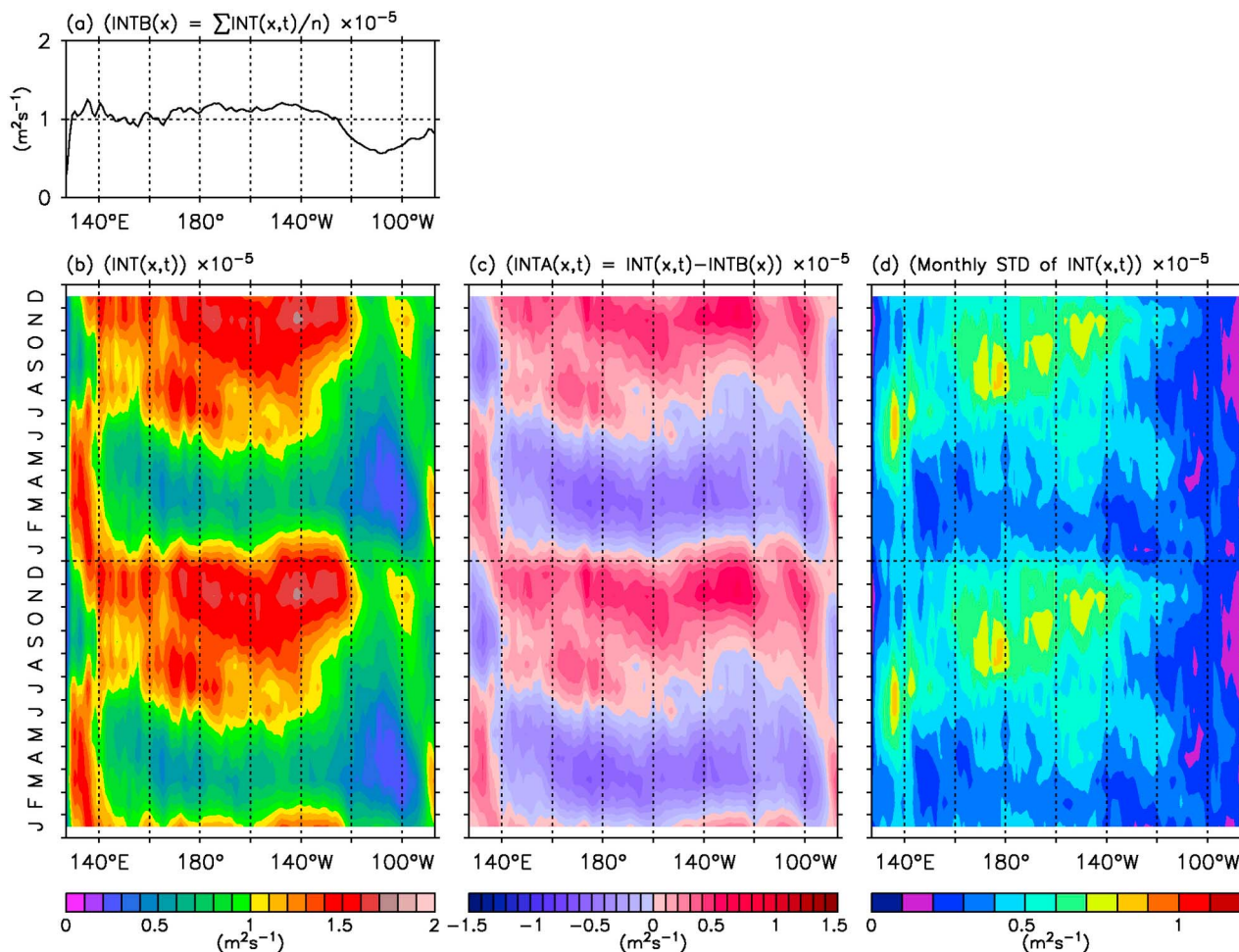


Figure 7. Same as Figure 6, but for the AVISO-U-based NECC intensity integrated meridionally from $\max(Y_{\text{CM}} - 4^\circ, 2^\circ\text{N})$ to $Y_{\text{CM}} + 4^\circ$.

Pacific. When a positive (negative) SSHA appears, Y_{CM} shifts to the north (south) of the mean pathway. This is so because a positive SSHA corresponds to an anomalous eastward flow on its poleward side and an anomalous westward flow on its equatorial side, and vice versa. In addition, a westward propagation of positive SSHA can be found around the NECC center. This positive SSHA forms in December–April and is confined to the region east of $\sim 100^\circ\text{W}$. Afterwards, it extends westward to the dateline at a speed of ~ 90 km/days from May to August. After September, it continues moving westward away from the dateline at a slower speed (~ 45 km/days) and stops around 150°E in November. The positive SSHA disappears after December and re-emerges during February–April. Similar westward propagation of a negative SSHA begins in May and ends in November.

[28] Comparing the SSHA field (Figure 8) with the W_{EK} field (Figure 9) reveals some correspondences between the seasonally varying Ekman pumping velocity field and the local sea surface height field. Following the NECC pathway, a strong positive W_{EK} exists east of 140°W and confines the positive SSHA to the region east of $\sim 100^\circ\text{W}$ during the period of January–April. After May, with a northward

intrusion of negative W_{EK} , which tends to induce a positive SSHA, from the equator, the positive SSHA moves westward quickly. This northward-moving negative W_{EK} begins around 100°W in May, extends westward up to the western Pacific by September, and shrinks back to the east afterwards. In December, the entire mean NECC pathway is covered by a positive W_{EK} . By January, this positive W_{EK} is interrupted by a southward intrusion of negative W_{EK} north of 10°N between 160°E and 130°W . During January–April, the broken positive W_{EK} in the eastern Pacific moves southward to prevent the newly formed positive SSHA east of $\sim 100^\circ\text{W}$ from propagating westward.

[29] The outcome showed in Figures 8 and 9 indicates that both W_{EK} and Rossby wave propagation are important in regulating the evolution of SSHA field and the meridional movement of the NECC center. *Kessler* [1990] suggested that the wave-dominated variability (westward long Rossby wave) at 5°N weakens the annual cycle of the geostrophic transport of NECC in the western Pacific but the Ekman pumping causes the annual cycle of 20°C isotherm in the eastern and central Pacific. His result implies that the dynamical explanation for the behavior of NECC in the western Pacific could be different from that in the central

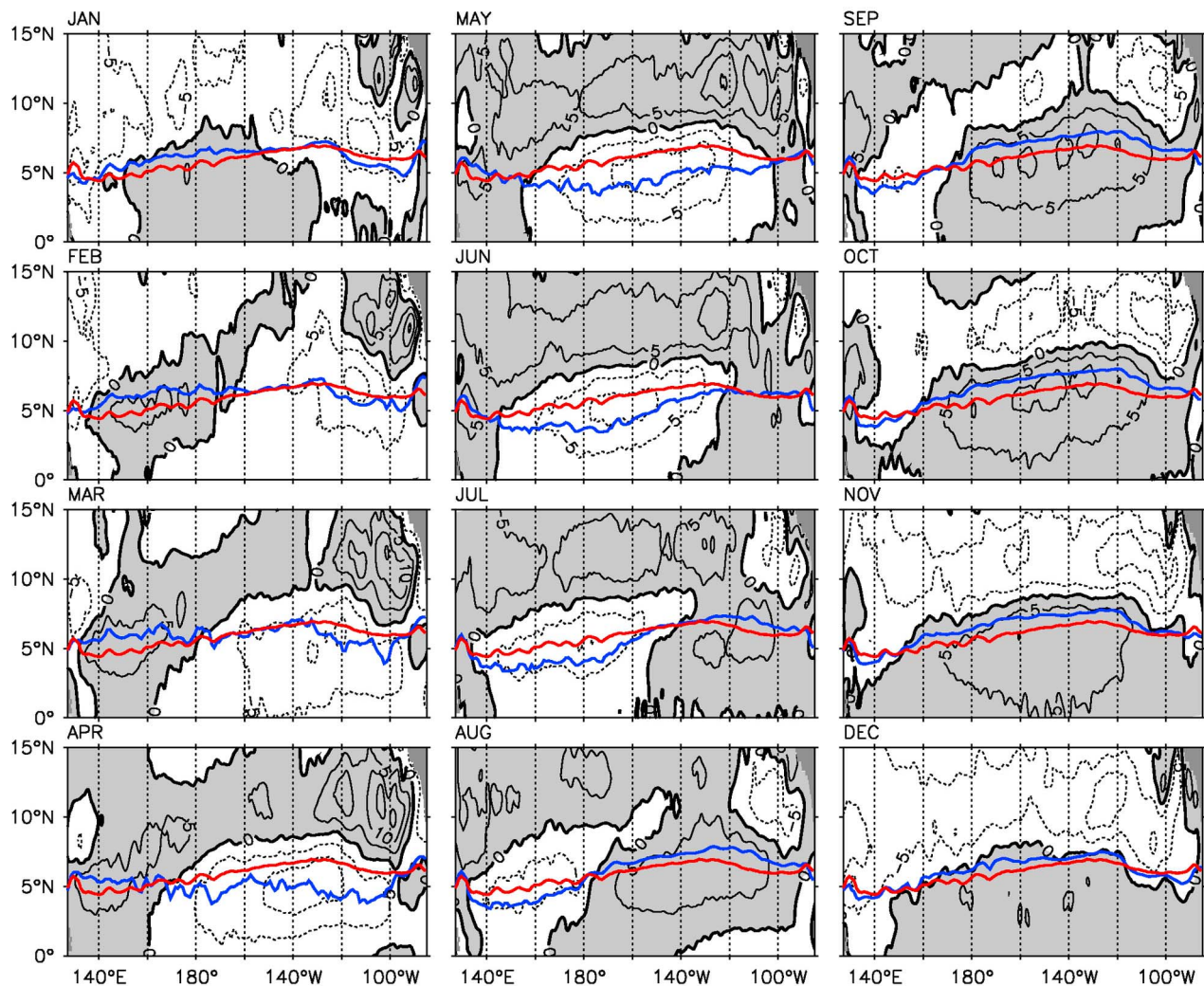


Figure 8. Annual march of AVISO-SSHA. Gray shading represents positive SSHA and contour interval is 5 cm. Red curve is the annual mean OSCAR-U-based Y_{CM} , and blue one depicts the OSCAR-U-based Y_{CM} for each month.

and eastern Pacific. Therefore, a wind-driven first-mode baroclinic Rossby wave model, which combines the wind-forcing and Rossby wave motion together, can be a useful tool in discussing the relevant mechanisms for the NECC variability.

[30] In order to utilize the linear wind-driven first-mode baroclinic Rossby wave model presented in equation (5), it is necessary to determine appropriate ε and g' values for the area of our study. By minimizing the difference between the AVISO-SSHA and modeled SSHA along each latitude (equation (7)), Figures 10a and 10b show the optimal latitude-varying ε and g' values encompassing the NECC region. Between 2°N and 10°N, the optimal ε ranges from 1/0.1 yr to 1/0.3 yr with an average of about 1/0.2 yr. The ε value in general decreases poleward. In terms of the optimal g' value, it ranges between 0.02 and 0.08 ms^{-2} with an average of about 0.045 ms^{-2} . The optimal g' value has local minima around 2°N–4°N and 9°N–12°N while it has a local

maximum in between. A large (small) g' value signifies a large (small) density difference across the base of the main thermocline. As suggested by previous studies, the maximal and minimal g' values south of 10°N correspond to the thermocline ridge and trough, respectively [e.g., Kessler, 1990; Donguy and Meyers, 1996; Johnson *et al.*, 2002].

[31] In the following, we force the first-mode baroclinic Rossby wave model with the optimal latitude-varying ε and g' values shown in Figures 10a and 10b. This case is denoted as CTL in Table 1. Figure 10c shows the spatial distribution of correlation coefficient between the AVISO-SSHA and the modeled SSHA of CTL. The correlation coefficient is larger than 0.5 in most of the studied areas, except for the central Pacific (180°W–120°W) and the eastern Pacific (east of 100°W), implying that the SSHA fluctuations in these two areas are not adequately explained by the first-mode baroclinic Rossby wave model. The poor correlation in the central Pacific could be ascribed to factors such as the

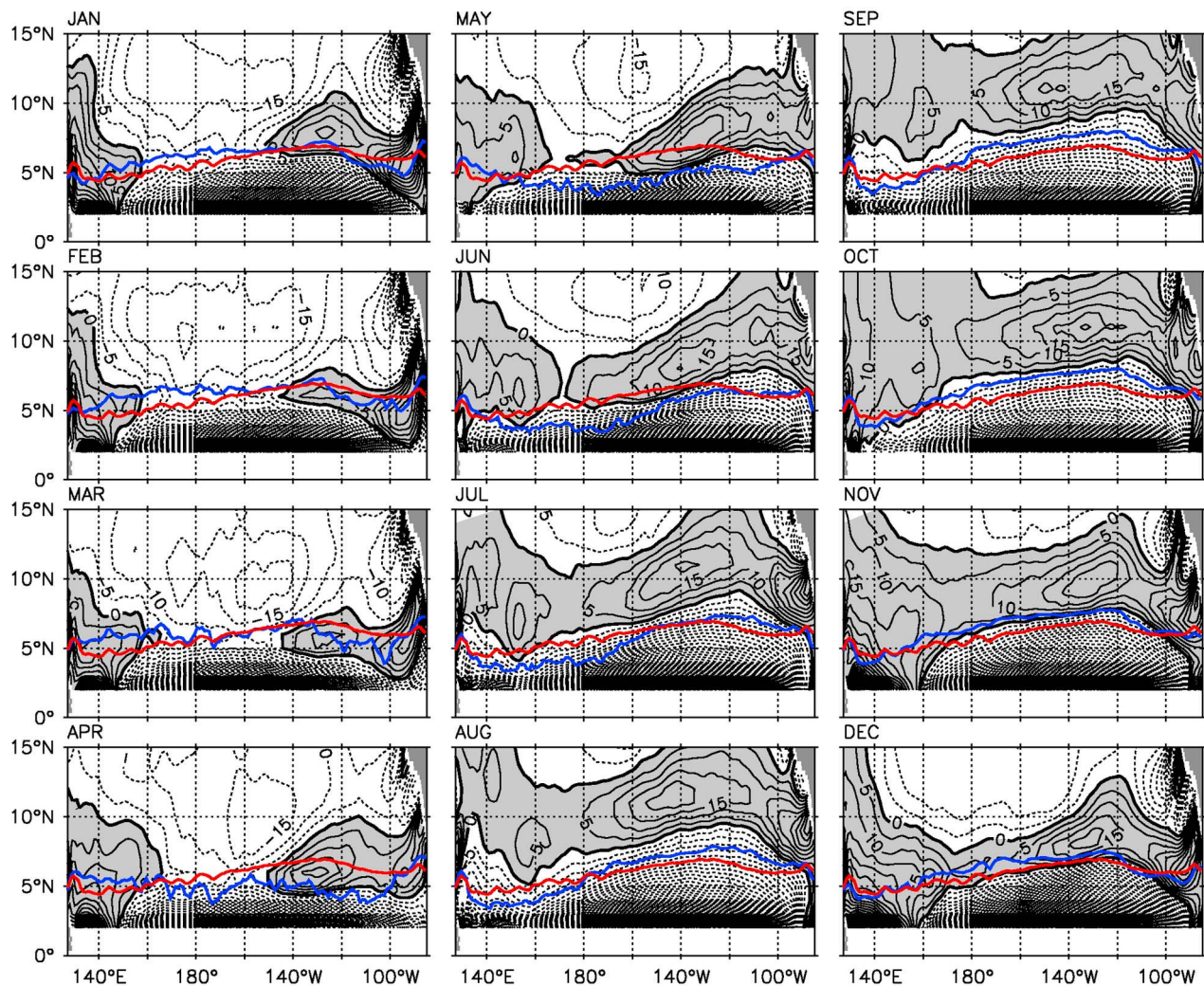


Figure 9. Annual march of Ekman pumping velocity ($5 \cdot 10^6 \cdot \frac{1}{\rho_0} \cdot \nabla \times \left(\frac{\bar{\tau}}{f} \right) \cdot \vec{k}$). Gray shading represents positive velocity. Red curve is the annual mean OSCAR-U-based Y_{CM} , and blue one depicts the OSCAR-U-based Y_{CM} for each month.

tropical instability waves, which are generated by nonlinear processes excluded from the Rossby wave model. The modeled SSHA signals along the eastern Pacific boundary can be improved when the boundary SSHA forcing is added to equation (6) [Fu and Qiu, 2002].

[32] Figure 11 shows the monthly distributions of modeled Y_{ACM} and $INTA$. These two quantities are derived from the modeled SSHA plus the RioMDT and averaged month-by-month over the period between January 1993 and December 2009. As shown in Figure 11a, the model reproduces the key features of the observed Y_{ACM} (Figure 5c): Y_{CM} shifts separately along its mean pathway west and east of the dateline. The modeled Y_{ACM} shows that a northward shift of NECC east (west) of the dateline starts in August (December) and stops in November (May). This outcome is consistent with the observed Y_{ACM} (Figure 5c). Concerning the intensity of NECC (Figure 11b), the model roughly captures the seasonal change of the observed NECC intensity (Figures 6c and 7c). With respect to the seasonal INT phase, the modeled NECC intensity is in general in

agreement with that of AVISO-U-based INT (Figure 7c). Two maxima, for example, are also revealed in the modeled INT .

[33] While some discrepancies exist between the modeled and observed Y_{ACM} and INT , their overall agreement allows us to further explore the different behavior of NECC east and west of the dateline. Five experiments, summarized in Table 1, are executed to clarify the roles of W_{EK} and first-mode baroclinic Rossby waves in modulating the seasonality of NECC center. Among these experiments, CTL, EX1, EX2, and EX3 are carried out to discuss the NECC movement east of the dateline. Comparing the results of CTL, EX1, EX4, and EX5 can help understand the NECC west of the dateline. The modeled Y_{ACM} for all experiments are shown in Figure 12.

[34] When setting the baroclinic Rossby wave speed to zero in the whole NECC area (EX1; that is, the second term on the left hand side of equation (5) is ignored), the modeled SSHA is totally determined by the local W_{EK} forcing shown in Figure 9. The Y_{ACM} in EX1 misses the key feature of

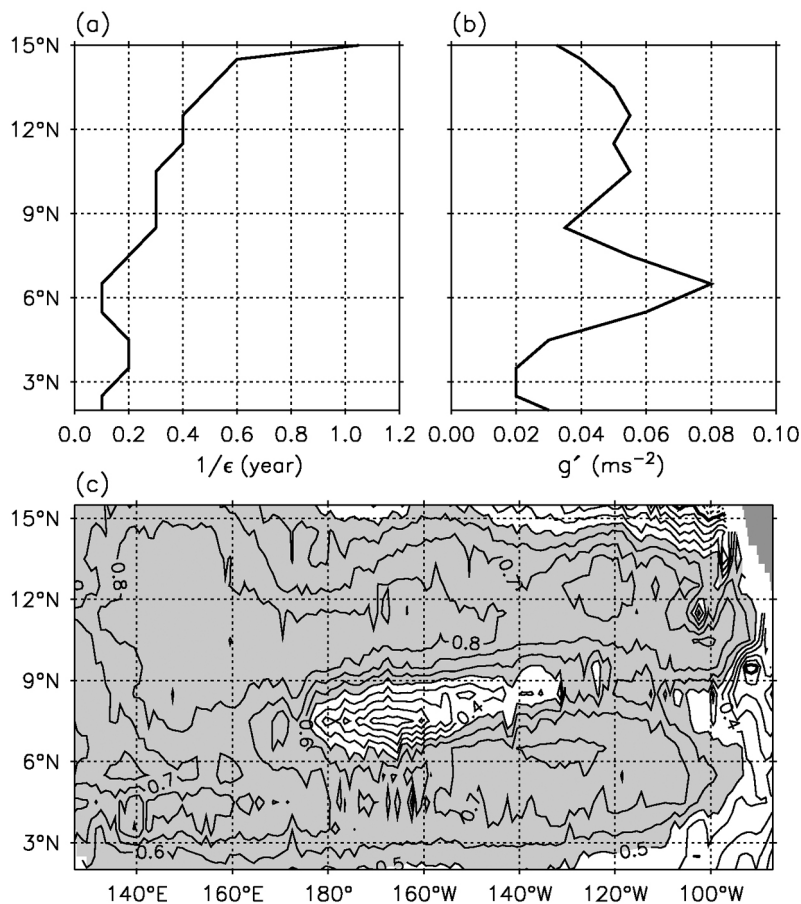


Figure 10. Latitude-specifics of (a) optimal Newtonian dissipation time ($1/\epsilon$, year) and (b) optimal g' (m s^{-2}). Forced the Rossby wave model with the optimal ϵ and g' , (c) the spatial distribution of correlation coefficient between the AVISO-SSHA and modeled SSHA is presented. Gray shading in Figure 10c highlights the correlation coefficient greater than 0.5.

NECC movement across the Pacific basin, implying that the Rossby wave effect is important for the entire Pacific NECC. In this experiment, the northward movement of Y_{CM} east of 160°E takes place twice in a year (spring and fall), and that west of 160°E occurs during October–May (Figure 12b). Regarding the NECC east of 160°E, its northward movement in spring is due to the southward invasion of negative W_{EK} from the higher latitude to the NECC region, while that in fall is attributable to the negative W_{EK} extending northward from the equator. In the western Pacific, the northward movement of NECC is ascribed to the strengthening of the negative W_{EK} in the vicinity of the western boundary.

[35] When the wave effect is added back to EX1 in the east of the dateline (EX2; Figure 12c), the seasonality of Y_{CM} simulated by the CTL run east of the dateline is replicated. However, when W_{EK} is removed over most of the Pacific (west of 100°W; Figure 12d), there is little agreement between the CTL and EX3 Y_{CM} seasonality. These model experiments suggest that both the variability of W_{EK} and the westward-propagating Rossby wave are important in modulating the pathway of the NECC center east of the dateline.

[36] EX4 and EX5 are performed to clarify the factors important for the seasonality of Y_{CM} west of the dateline.

When the wave effect is added back to EX1 in the west of the dateline (EX4; Figure 12e), the two northward shifts of Y_{CM} east of the dateline induced by the Ekman pumping (revealed in EX1) are extended to the west of the dateline by the transmission of Rossby waves. However, the seasonality of Y_{CM} west of the dateline is still mismatched in EX4. When the wave effect is added to EX2 (EX5; Figure 12f), the seasonal change of Y_{CM} west of the dateline recovers although in this experiment W_{EK} remains null in the west of the dateline. This result indicates that the seasonal shift of NECC center west of the dateline originates in the east of the dateline and is being conveyed westward by Rossby waves.

Table 1. Description of Model Experiments

Case	Description
CTL	Forced by ECMWF ORA-S3 wind stress curl with latitude-varying ϵ and g' in Figure 10, and $C_{\text{R}}(x, y) \neq 0$
EX1	Same as CTL, but with $C_{\text{R}} = 0$ in the full domain
EX2	Same as CTL, but with $C_{\text{R}} = 0$ west of the dateline
EX3	Same as CTL, but with $W_{\text{EK}} = 0$ west of 100°W
EX4	Same as CTL, but with $C_{\text{R}} = 0$ east of the dateline
EX5	Same as CTL, but with $W_{\text{EK}} = 0$ west of the dateline

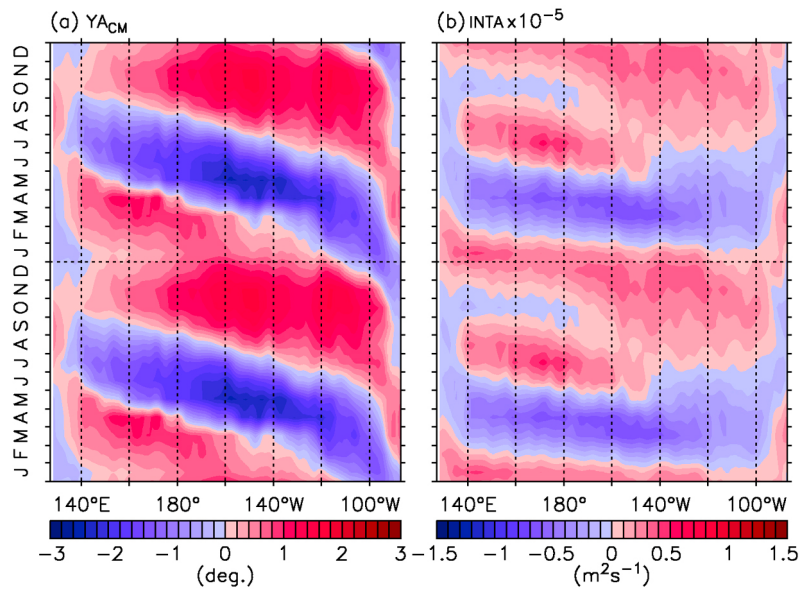


Figure 11. Monthly distribution of anomalies of (a) Y_{CM} , and (b) NECC intensity simulated from the Rossby wave model with the optimal ε and g' values in Figure 10. The modeled SSHA plus the mean dynamic topography [Rio and Hernandez, 2004] is used to derive these anomalies.

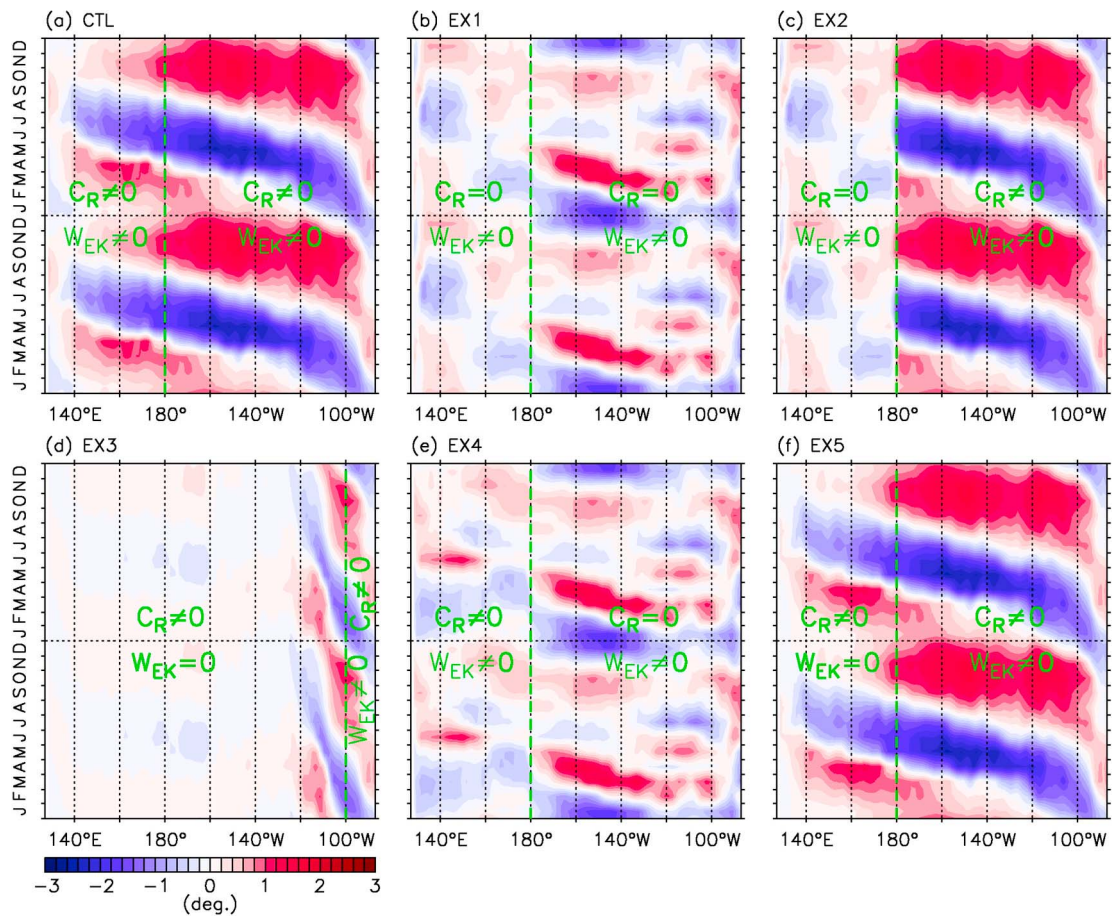


Figure 12. Monthly distribution of modeled Y_{CM} anomaly for model experiments summarized in Table 1. The corresponding C_R and W_{EK} are labeled.

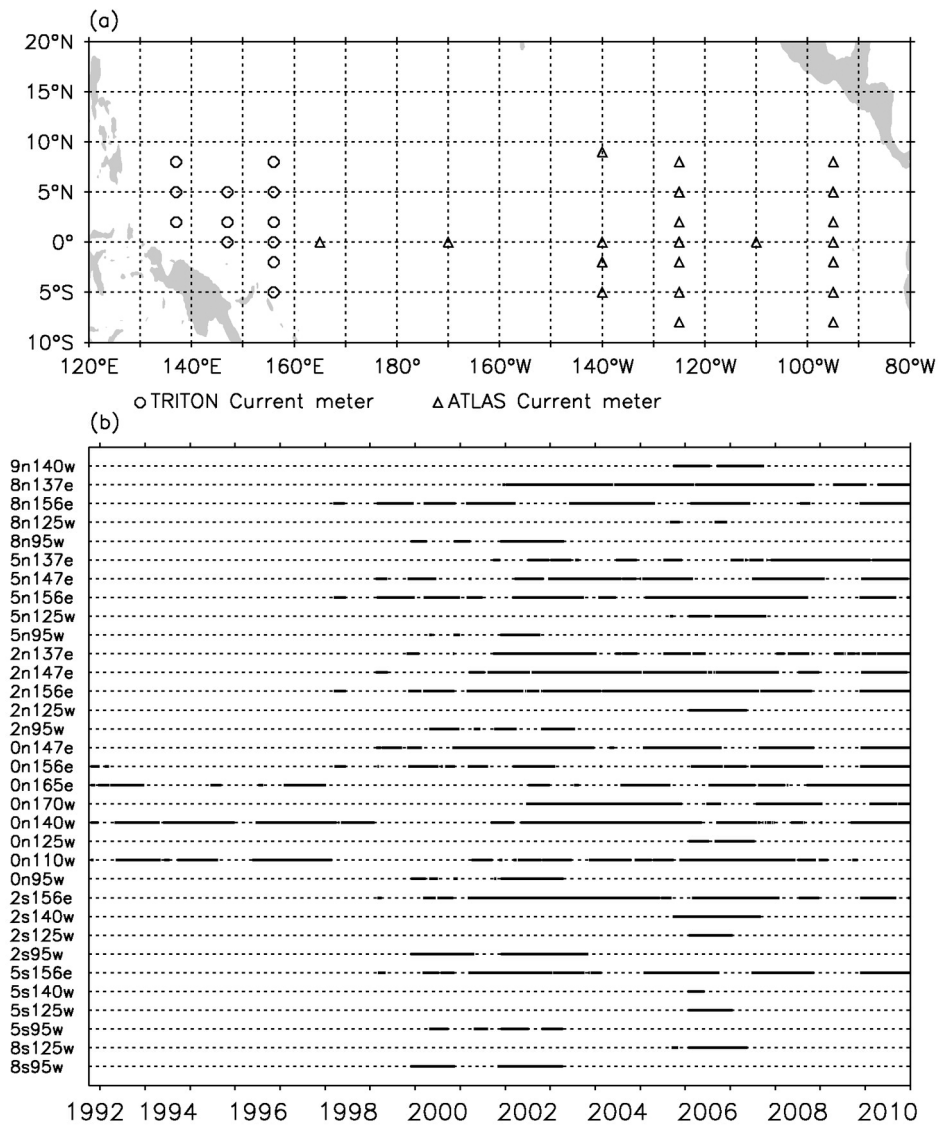


Figure A1. Location and executed duration for current meters of TAO/TRITON moorings during October 1992 to December 2010.

In other words, in the western Pacific, the Rossby wave effect dominates the seasonality of NECC, with the Ekman pumping only playing a secondary role. In addition to the above mentioned factors, *Brown et al.* [2010] have recently suggested that eddies are important in driving and

positioning the NECC in the western equatorial Pacific. By strengthening the NECC, eddies can move its center closer to the equator via nonlinear effects. Although these nonlinear processes are not included in the Rossby wave model, we

Table A1. Correlation Coefficients of Zonal Velocity, U, Between TAO/TRITON Moored Current, at 10 m, and OSCAR Current, at 15 m^a

	137°E	147°E	156°E	165°E	170°W	140°W	125°W	110°W	95°W
9°N						0.96/0.94			
8°N	0.72/0.83		0.77/0.81				0.86/0.87		0.92/0.89
5°N	0.80/0.83	0.84/0.88	0.85/0.87				0.74/0.78		0.68/0.66
2°N	0.79/0.80	0.84/0.83	0.87/0.87				0.85/0.79		0.70/0.61
0°		0.66/0.74	0.82/0.85	0.76/0.81	0.64/0.70	0.58/0.66	0.82/0.84	0.67/0.73	0.34/0.37
2°S			0.80/0.80			0.82/0.85	0.82/0.75		0.50/0.49
5°S			0.71/0.75			0.74/0.72	0.76/0.85		0.69/0.70
8°S							0.87/0.84		0.69/0.60

^aGiven in format of 1/3°/1°. Bolding indicate when the correlation of 1° OSCAR is higher than that of 1/3° OSCAR.

Table A2. Correlation Coefficients of Meridional Velocity, V , Between TAO/TRITON Moored Current, at 10 m, and OSCAR Current, at 15 m^a

	137°E	147°E	156°E	165°E	170°W	140°W	125°W	110°W	95°W
9°N						0.81/0.84			
8°N	0.64/0.71		0.56/0.53				0.86/0.91		0.79/0.76
5°N	0.75/0.82	0.69/0.75	0.52/0.59				0.56/0.68		0.68/0.74
2°N	0.21/0.22	0.38/0.48	0.33/0.44				0.38/0.50		0.50/0.38
0°		0.09/0.03	0.10/0.22	0.11/0.18	0.10/0.14	0.16/0.24	0.28/0.31	0.22/0.33	0.07/0.22
2°S			0.32/0.33			0.40/0.54	0.67/0.68		0.26/0.43
5°S			0.64/0.62			0.71/0.82	0.61/0.75		0.67/0.71
8°S							0.51/0.49		0.57/0.53

^aGiven in format of $1/3^\circ/1^\circ$. Bolding indicate when the correlation of 1° OSCAR is higher than that of $1/3^\circ$ OSCAR.

are still able to explain the key features of the observed seasonality.

6. Conclusions

[37] Thanks to the progress in the satellite technique and data accumulation, the satellite-based data can serve as a useful tool to re-investigate the ocean currents in the surface layer. With the combined use of the Ocean Surface Current Analysis – Real Time data and altimeter-based data (sea surface height anomaly and geostrophic current), the seasonality of surface NECC across the entire Pacific basin are explored in this study, including its central position and intensity. One of the new findings is that the central position of NECC east and west of the dateline shifts northward in different periods. Y_{CM} east of the dateline moves northward in the latter half of a year while that west of the dateline shifts to the north in the first half of a year. Both Y_{CM} east and west of the dateline have westward-propagating signals. Furthermore, the seasonality of the NECC center agrees well with the sea surface height changes along its pathway. A positive/negative sea surface height anomaly accompanies a northward/southward movement of the NECC center. In terms of the NECC intensity, the NECC strengthens (weakens) in the latter (first) half of a year. The seasonal change of NECC intensity is primarily controlled by the geostrophic current signals; other factors such as the Ekman dynamic play a minor role.

[38] By means of a linear wind-driven first-mode baroclinic Rossby wave model, the mechanism of the meridional movement of NECC is addressed. The model driven by Ekman pumping can well reproduce the evolution of sea surface height change and the two modes of northward shifts of the NECC center. The seasonality of the NECC center east of the dateline is regulated by both the forcing of Ekman

pumping and the westward propagating Rossby waves, whereas in the west of the dateline it is mainly determined by Rossby waves that originate in the east of the dateline. Ekman pumping plays a minor role in influencing the central position of the NECC west of the dateline.

Appendix A: Comparison of OSCAR with TAO/TRITON array

[39] Some quantitative validations have been made for the 1° version OSCAR product by *Bonjean and Lagerloef* [2002] and *Johnson et al.* [2007] using available observational data from free-flowing surface drifters, moored current meters, and shipboard ADCP. These investigations were mostly focused on the eastern and central parts of the tropical Pacific Ocean, and careful comparisons in the western part are lacking. *Johnson et al.* [2007] divided the Pacific Ocean between 30°S and 30°N into nine sub-areas and correlated the 1° OSCAR with currents derived from surface drifters in each sub-area. The correlation coefficient for zonal velocity is always higher (0.52–0.86) than that for meridional velocity (0.36–0.59). Spatially, the correlation coefficients of zonal velocity in the central and eastern parts (>0.85) are higher than in the western part (0.69). Close to the equator, the correlation of meridional velocity is much lower (0.36–0.47). This low correlation was also noted in the initial study of OSCAR by *Bonjean and Lagerloef* [2002] and for another ocean surface current product developed by the Centre of Topography of the Oceans and the Hydrosphere in France [*Sudre and Morrow*, 2008].

[40] Although the comparisons for the 1° OSCAR have shown that the OSCAR is adequate for the investigation of the surface current in the tropical Pacific Ocean, we carry out careful validations for the latest OSCAR product with the Tropical Atmosphere Ocean/Triangle Trans-Ocean Buoy

Table A3. RMSD Between Zonal Velocity, U , Between TAO/TRITON Moored Current, at 10 m, and OSCAR Current, at 15 m (in cm s^{-1})^a

	137°E	147°E	156°E	165°E	170°W	140°W	125°W	110°W	95°W
9°N						9/8			
8°N	12/10		10/8				9/9		10/12
5°N	16/14	13/10	11/9				15/15		12/11
2°N	49/52	30/33	22/25				29/42		24/31
0°		45/54	30/24	39/31	28/27	39/33	33/30	38/34	37/32
2°S			24/19			20/18	17/20		31/29
5°S			16/12			9/10	9/6		16/9
8°S							5/7		6/7

^aGiven in format of $1/3^\circ/1^\circ$. Bolding indicate when the correlation of 1° OSCAR is higher than that of $1/3^\circ$ OSCAR.

Table A4. RMSD Between Meridional Velocity, V, Between TAO/TRITON Moored Current, at 10 m, and OSCAR Current, at 15 m (in cm s^{-1})^a

	137°E	147°E	156°E	165°E	170°W	140°W	125°W	110°W	95°W
9°N						7/7			
8°N	14/11		15/11				7/6		10/11
5°N	16/11	15/11	13/10				20/19		12/10
2°N	44/20	24/15	33/15				22/15		23/18
0°		29/19	33/22	31/19	25/17	33/26	36/31	35/28	31/23
2°S			25/17			23/15	18/19		22/17
5°S			14/12			11/10	8/7		10/9
8°S							8/8		6/6

^aGiven in format of $1/3^\circ/1^\circ$. Bolding indicate when the correlation of 1° OSCAR is higher than that of $1/3^\circ$ OSCAR.

Network (TAO/TRITON) array in order to assess if the $1/3^\circ$ OSCAR is superior than the 1° OSCAR. In the tropical Pacific Ocean, the TAO/TRITON mooring array provides a network of monitoring the multiscale variability of air-sea parameters in the equatorial Pacific region [McPhaden *et al.*, 1998]. Here, we utilize the current meter data at 10-m depth during the period of October 1992 to September 2010. Figure A1 shows the locations and execution durations of available current meters. As shown in Figure A1b, except for the four moorings at 156°E , 165°E , 140°W , and 110°W at the equator implemented before 1998, most of data are available during the period of 1998–2010, and all data are scattered temporally. Despite of the data gaps, the TAO/TRITON mooring data remains the best data set available to validate and examine the satellite-derived OSCAR results. The current meter data are obtained from the TAO website: <http://www.pmel.noaa.gov/tao>.

[41] Tables A1 and A2 summarize the correlation coefficients between $1/3^\circ$ and 1° surface current from the OSCAR and TAO/TRITON moorings for the zonal (U) and meridional (V) components, respectively. The OSCAR data are linearly interpolated to the locations of each mooring station for correlation analysis. The correlation coefficients of both velocity components increase poleward. Also, the correlation of U is larger than V, confirming the conclusion reached by Johnson *et al.* [2007]. The overall correlation coefficients for both U and V are quite high in the NECC region (2°N – 10°N), especially for U, suggesting that the new version OSCAR data are suitable to study the variability of NECC. Moreover, such a high correlation is also found in the southern Pacific. By comparing the correlation coefficients of both versions of OSCAR data, those of the 1° OSCAR seem to be better. In addition to the correlation coefficient, the root mean square difference (RMSD) between the TAO/TRITON moored current and the OSCAR current is also calculated in Tables A3 and A4 to evaluate the two versions of OSCAR data. At most of mooring stations, RMSDs of the 1° OSCAR are less than those of the $1/3^\circ$ OSCAR. In summary, by comparing the correlation coefficient and RMSD between the two versions, the performance of $1/3^\circ$ OSCAR is not improved with its improvement of spatial resolution. Hence, we will use the 1° version OSCAR product in presenting the seasonal changes of central position and intensity of the NECC.

[42] **Acknowledgments.** This research is supported by grant N00014-10-1-0267 of ONR and by contract 1207881 from JPL as part of the NASA Ocean Surface Topography Mission.

References

- Ando, K., and T. Hasegawa (2009), Annual zonal displacement of Pacific warm pool in association with El Niño onset, *SOLA*, 5, 149–152, doi:10.2151/sola.2009-038.
- Balmaseda, M. A., A. Vidard, and D. L. T. Anderson (2008), The ECMWF ocean analysis system: ORA-S3, *Mon. Weather Rev.*, 136, 3018–3034, doi:10.1175/2008MWR2433.1.
- Bonjean, F., and G. S. E. Lagerloef (2002), Diagnostic model and analysis of the surface currents in the tropical Pacific Ocean, *J. Phys. Oceanogr.*, 32, 2938–2954, doi:10.1175/1520-0485(2002)032<2938:DMAAOT>2.0.CO;2.
- Brown, J. N., J. S. Godfrey, and A. Schiller (2007), A discussion of flow pathways in the central and eastern Equatorial Pacific, *J. Phys. Oceanogr.*, 37, 1321–1339, doi:10.1175/JPO3042.1.
- Brown, J. N., J. S. Godfrey, and S. E. Wijffels (2010), Nonlinear effects of tropical instability waves on the Equatorial Pacific Circulation, *J. Phys. Oceanogr.*, 40, 381–393, doi:10.1175/2009JPO3963.1.
- Chelton, D. B., R. A. deSzoeke, M. G. Schlax, K. El Naggar, and N. Siwertz (1998), Geographical variability of the first-baroclinic Rossby radius of deformation, *J. Phys. Oceanogr.*, 28, 433–460, doi:10.1175/1520-0485(1998)028<0433:GVOTFB>2.0.CO;2.
- Chelton, D. B., M. G. Schlax, J. M. Lyman, and G. C. Johnson (2003), Equatorially trapped Rossby waves in the presence of meridionally sheared baroclinic flow in the Pacific Ocean, *Prog. Oceanogr.*, 56, 323–380, doi:10.1016/S0079-6611(03)00008-9.
- Chen, S., and B. Qiu (2004), Seasonal variability of the South Equatorial Countercurrent, *J. Geophys. Res.*, 109, C08003, doi:10.1029/2003JC002243.
- Coles, V. J., and M. M. Rienecker (2001), North Pacific subtropical-tropical gyre exchanges in the thermocline: Simulations with two isopycnic OGCMs, *J. Phys. Oceanogr.*, 31, 2590–2611, doi:10.1175/1520-0485(2001)031<2590:NPSTGE>2.0.CO;2.
- Delcroix, T., G. Eldin, and C. Henin (1987), Upper ocean water masses and transports in the western tropical Pacific (165°E), *J. Phys. Oceanogr.*, 17, 2248–2262, doi:10.1175/1520-0485(1987)017<2248:UOWMAT>2.0.CO;2.
- Delcroix, T., J. Picaut, and G. Eldin (1991), Equatorial Kelvin and Rossby waves evidenced in the Pacific Ocean through Geosat sea level and surface current anomalies, *J. Geophys. Res.*, 96, 3249–3262.
- Delcroix, T., G. Eldin, M.-H. Radenac, J. Toole, and E. Firing (1992), Variation of the western equatorial Pacific Ocean, 1986–1988, *J. Geophys. Res.*, 97(C4), 5423–5445, doi:10.1029/92JC00127.
- Donguy, J.-R., and G. Meyers (1996), Mean annual variation of transport of major currents in the tropical Pacific Ocean, *Deep Sea Res., Part I*, 43(7), 1105–1122, doi:10.1016/0967-0637(96)00047-7.
- Fu, L.-L., and B. Qiu (2002), Low-frequency variability of the North Pacific Ocean: The roles of boundary- and wind-driven baroclinic Rossby waves, *J. Geophys. Res.*, 107(C12), 3220, doi:10.1029/2001JC001131.
- Gouriou, Y., and J. Toole (1993), Mean circulation of the upper layers of the western equatorial Pacific Ocean, *J. Geophys. Res.*, 98(C12), 22,495–22,520, doi:10.1029/93JC02513.
- Heron, S. F., E. J. Metzger, and W. J. Skirving (2006), Seasonal variations of the ocean surface circulation in the vicinity of Palau, *J. Oceanogr.*, 62(4), 413–426, doi:10.1007/s10872-006-0065-3.
- Johnson, E. S., F. Bonjean, G. S. E. Lagerloef, J. T. Gunn, and G. T. Mitchum (2007), Validation and error analysis of OSCAR sea surface currents, *J. Atmos. Oceanic Technol.*, 24(4), 688–701, doi:10.1175/JTECH1971.1.
- Johnson, G. C., B. M. Sloyan, W. S. Kessler, and K. E. McTaggart (2002), Direct measurements of upper ocean currents and water properties across the tropical Pacific during the 1990s, *Prog. Oceanogr.*, 52(1), 31–61, doi:10.1016/S0079-6611(02)00021-6.

- Kessler, W. S. (1990), Observation of long Rossby waves in the northern tropical Pacific, *J. Geophys. Res.*, *95*(C4), 5183–5217, doi:10.1029/JC095iC04p05183.
- Kessler, W. S. (2006), The circulation of the eastern tropical Pacific: A review, *Prog. Oceanogr.*, *69*(2–4), 181–217, doi:10.1016/j.pcean.2006.03.009.
- Lukas, R., E. Firing, P. Hacker, P. L. Richardson, C. A. Collins, R. Fine, and R. Gammon (1991), Observations of the Mindanao Current during the Western Equatorial Pacific Ocean Circulation Study, *J. Geophys. Res.*, *96*(C4), 7089–7104, doi:10.1029/91JC00062.
- Masunaga, H., and T. S. L'Ecuyer (2011), Equatorial asymmetry of the east Pacific ITCZ: Observational constraints on the underlying processes, *J. Clim.*, *24*, 1784–1800, doi:10.1175/2010JCLI3854.1.
- McPhaden, M. J. (1996), Monthly period oscillations in the Pacific North Equatorial Countercurrent, *J. Geophys. Res.*, *101*(C3), 6337–6359, doi:10.1029/95JC03620.
- McPhaden, M. J., et al. (1998), The Tropical Ocean Global Atmosphere observing system: A decade of progress, *J. Geophys. Res.*, *103*(C7), 14,169–14,240, doi:10.1029/97JC02906.
- Meyers, G. (1979), On the annual Rossby wave in the tropical North Pacific Ocean, *J. Phys. Oceanogr.*, *9*(4), 663–674, doi:10.1175/1520-0485(1979)009<0663:OTARW>2.0.CO;2.
- Perez, R. C., D. B. Chelton, and R. N. Miller (2005), The effects of wind forcing and background mean currents on the latitudinal structure of equatorial Rossby waves, *J. Phys. Oceanogr.*, *35*(5), 666–682, doi:10.1175/JPO2714.1.
- Philander, S. G. H., W. J. Hurlin, and A. D. Seigel (1987), Simulation of the seasonal cycle of the tropical Pacific Ocean, *J. Phys. Oceanogr.*, *17*(11), 1986–2002, doi:10.1175/1520-0485(1987)017<1986:SOTSCO>2.0.CO;2.
- Qiao, L., and R. H. Weisberg (1995), Tropical instability wave kinematics: Observations from the Tropical Instability Wave Experiment, *J. Geophys. Res.*, *100*(C5), 8677–8693, doi:10.1029/95JC00305.
- Qiu, B., and S. Chen (2010), Interannual-to-decadal variability in the bifurcation of the North Equatorial Current off the Philippines, *J. Phys. Oceanogr.*, *40*(11), 2525–2538, doi:10.1175/2010JPO4462.1.
- Qiu, B., and S. Chen (2012), Multidecadal sea level and gyre circulation variability in the northwestern tropical Pacific Ocean, *J. Phys. Oceanogr.*, *42*(1), 193–206, doi:10.1175/JPO-D-11-061.1.
- Qiu, B., and T. M. Joyce (1992), Interannual variability in the mid- and low-latitude western North Pacific, *J. Phys. Oceanogr.*, *22*(9), 1062–1079, doi:10.1175/1520-0485(1992)022<1062:IVITMA>2.0.CO;2.
- Qiu, B., and R. Lukas (1996), Seasonal and interannual variability of the North Equatorial Current, the Mindanao Current and the Kuroshio along the Pacific western boundary, *J. Geophys. Res.*, *101*(C5), 12,315–12,330, doi:10.1029/95JC03204.
- Qiu, B., M. Mao, and Y. Kashino (1999), Intraseasonal variability in the Indo-Pacific Throughflow and the regions surrounding the Indonesian Seas, *J. Phys. Oceanogr.*, *29*(7), 1599–1618, doi:10.1175/1520-0485(1999)029<1599:IVITIP>2.0.CO;2.
- Reverdin, G., C. Frankignoul, E. Kestenare, and M. J. McPhaden (1994), Seasonal variability in the surface currents of the equatorial Pacific, *J. Geophys. Res.*, *99*(C10), 20,323–20,344, doi:10.1029/94JC01477.
- Reynolds, R. W., N. A. Rayner, T. M. Smith, D. C. Stokes, and W. Wang (2002), An improved in situ and satellite SST analysis for climate, *J. Clim.*, *15*(13), 1609–1625, doi:10.1175/1520-0442(2002)015<1609:AIISAS>2.0.CO;2.
- Richards, K. J., S.-P. Xie, and T. Miyama (2009), Vertical mixing in the ocean and its impact on the coupled ocean-atmosphere system in the eastern tropical Pacific, *J. Clim.*, *22*, 3703–3719, doi:10.1175/2009JCLI2702.1.
- Rio, M. H., and F. Hernandez (2004), A mean dynamics topography computed over the world ocean from altimetry, in situ measurements, and a geoid model, *J. Geophys. Res.*, *109*, C12032, doi:10.1029/2003JC002226.
- Sprintall, J., S. Kennan, Y. Y. Kim, and P. Niiler (2009), Wind-driven ageostrophic transport in the North Equatorial Countercurrent of the eastern Pacific at 95°W, *J. Phys. Oceanogr.*, *39*, 2985–2998, doi:10.1175/2009JPO4088.1.
- Sudre, J., and R. A. Morrow (2008), Global surface currents: A high-resolution product for investigating ocean dynamics, *Ocean Dyn.*, *58*(2), 101–118, doi:10.1007/s10236-008-0134-9.
- Toole, J. M., E. Zou, and R. C. Millard (1988), On the circulation of the upper waters in the western equatorial Pacific Ocean, *Deep Sea Res., Part A*, *35*(9), 1451–1482, doi:10.1016/0198-0149(88)90097-0.
- White, W. B. (1977), Annual forcing of baroclinic long waves in the tropical north Pacific Ocean, *J. Phys. Oceanogr.*, *7*(1), 50–61, doi:10.1175/1520-0485(1977)007<0050:AFOBLW>2.0.CO;2.
- Wyrtki, K. (1974), Sea level and the seasonal fluctuations of the equatorial currents in the western Pacific Ocean, *J. Phys. Oceanogr.*, *4*(1), 91–103, doi:10.1175/1520-0485(1974)004<0091:SLATSF>2.0.CO;2.
- Wyrtki, K., and R. Kendall (1967), Transports of the Pacific equatorial countercurrent, *J. Geophys. Res.*, *72*(8), 2073–2076, doi:10.1029/JZ072i008p02073.
- Yu, X., and M. J. McPhaden (1999), Seasonal variability in the equatorial Pacific, *J. Phys. Oceanogr.*, *29*(5), 925–947, doi:10.1175/1520-0485(1999)029<0925:SVITEP>2.0.CO;2.
- Yu, Z., J. P. McCreary Jr., W. S. Kessler, and K. A. Kelly (2000), Influence of equatorial dynamics on the Pacific North Equatorial Countercurrent, *J. Phys. Oceanogr.*, *30*(12), 3179–3190, doi:10.1175/1520-0485(2000)030<3179:IOEDOT>2.0.CO;2.